ICAS-88-5.4.2

STUDY OF THREE-DIMENSIONAL EFFECTS ON VORTEX BREAKDOWN

*M.D. Salas**

NASA Langley Research Center
Hampton, VA 23666-5225 USA

and

*G. Kuruvila***

Vigyan Research Associates, Inc.
Hampton, VA 23666-1325 USA

Abstract

The incompressible, axisymmetric, steady Navier-Stokes equations in primitive variables are used to simulate vortex breakdown. The equations, discretized using a second-order, central-difference scheme, are linearized and then solved using an exact LU decomposition, Gaussian elimination, and Newton iteration. Solutions are presented for Reynolds numbers, based on vortex-core radius, as high as 1500. An attempt to study the stability of the axisymmetric solutions to three-dimensional perturbations is discussed.

Introduction

Thirty years ago, Peckham and Atkinson[1] observed that under certain conditions the concentrated vortex core shed by the leading edge of the Gothic wing they were testing would swell, eventually stagnating the flow along the vortex axis and forming a bubble of reverse flow. Immediately downstream of the bubble the flow became highly unsteady and turbulent. The phenomenon was so striking that it became known as "vortex breakdown." The severe adverse effect of vortex breakdown on the performance of a wing has stimulated many experimental and theoretical studies. Comprehensive reviews of the progress made in understanding and predicting the occurrence of vortex breakdown have been given by Hall[2] and Leibovich.[3,4] With these works as background, it is only necessary here to review some of the salient features of the problem pertinent to this work.

Perhaps the single most important contribution to the study of vortex breakdown was made by Harvey[5], who isolated the vortex from the wing, and thus, set the stage for most of the "clean" experimental work that followed. Experimentally, Leibovich[4] identified two major types of breakdown; the "bubble" which appears as a basically axisymmetric phenomenon, and the "spiral" which characteristically represents a major departure from axial symmetry.

Theoretically and numerically, the bubble breakdown is the only one that has been studied in detail. The prevalent theory for the onset of breakdown is principally due to Benjamin.[6] In Benjamin's theory, breakdown is explained as a transition between a supercritical upstream flow incapable of supporting upstream propagating waves and a subcritical flow which allows upstream and downstream propagating waves. The theory is based on an inviscid quasi-cylindrical approximation which neglects all axial gradients. In general, no consistent correlation has been found between the occurrence of breakdown in the few available numerical solutions of the Navier-Stokes equations and the criticality condition of Benjamin.

Grabowski and Berger,[7] using Chorin's artificial compressibility method and a primitive variable formulation, calculated the first numerical solutions of the steady axisymmetric Navier-Stokes equations for this problem. Their work clearly established the existence of solutions with bubble-like breakdown under the axisymmetric assumption. However, the numerical scheme had difficulties in realizing fully-converged solutions and in obtaining solutions for Reynolds numbers, based on vortex-core radius, greater than 200. In reference 8, Hafez et al., using upwind differences and vertical line relaxation, solved the Navier-Stokes equations using the streamfunction - vorticity formulation and confirmed the earlier results of Grabowski and Berger. In order to overcome the 200 Reynolds number barrier encountered by Grabowski and Berger, Hafez et al.,[9] Salas et al.[10] and Beren,[11] each working independently, attacked the problem using direct matrix inversion techniques.

Encouraged by the success of this technique, this effort was directed towards solving the full three-dimensional problem. As a first step towards this goal, the axisymmetric Navier-Stokes equations in the primitive variable form were solved. In the current work, we present the results of the primitive variable formulation and address some issues related to the three-dimensional problem.

---

* Head, Theoretical Aerodynamics Branch, Transonic Aerodynamics Division.

** Research Engineer.

Mathematical Model

The governing equations are the Navier-Stokes equations. The flow is assumed to be steady, laminar and incompressible. The non-dimensional equations describing this flow, written in cylindrical coordinates, are

$$u_r + \frac{v_\theta}{r} + w_x + \frac{u}{r} = 0 \tag{1}$$

$$\mathbf{q}\cdot\nabla u - \frac{v^2}{r} + p_r = \frac{1}{Re}\left[\nabla^2 u - \frac{(u+2v_\theta)}{r^2}\right] \tag{2}$$

$$\mathbf{q}\cdot\nabla v + \frac{uv}{r} + \frac{p_\theta}{r} = \frac{1}{Re}\left[\nabla^2 v + \frac{(2u_\theta - v)}{r^2}\right] \tag{3}$$

$$\mathbf{q}\cdot\nabla w + p_x = \frac{1}{Re}\left[\nabla^2 w\right] \tag{4}$$

$$\mathbf{q} = u\hat{r} + v\hat{\theta} + w\hat{x} \tag{5}$$

$$\nabla = \frac{\partial}{\partial r}\hat{r} + \frac{1}{r}\frac{\partial}{\partial \theta}\hat{\theta} + \frac{\partial}{\partial x}\hat{x} \tag{6}$$

$$\nabla^2 = \frac{\partial^2}{\partial r^2} + \frac{1}{r}\frac{\partial}{\partial r} + \frac{1}{r^2}\frac{\partial^2}{\partial \theta^2} + \frac{\partial^2}{\partial x^2} \tag{7}$$

where u,v,w are the radial (r), azimuthal (θ), and axial (x) velocity components, respectively, and p is the pressure. Re is the Reynolds number defined in terms of the freestream axial velocity, the vortex-core radius, and the kinematic viscosity of the flow.

Numerical Scheme

Axisymmetric Problem

In the first part of this study, the axisymmetric assumption is retained. The four axisymmetric equations are linearized in the following manner. Let

$$\phi^{n+1} = \phi^n + \Delta\phi \tag{8}$$

where

$$\phi = [\,u, v, w, p\,]$$
$$\Delta\phi = [\,\Delta u, \Delta v, \Delta w, \Delta p\,]$$

Evaluating the four governing equations using the n+1 approximation and neglecting higher-order terms, we get a set of linear equations. These equations are discretized on a staggered rectangular mesh (Figure 1), where the variables v and p reside at the cell center and u and w reside at the middle of the horizontal and vertical cell faces respectively. The discretization uses a second-order central-difference formula. The continuity equation and the θ-momentum equation are discretized about the cell center. The other two momentum equations are discretized about appropriate cell faces.

Boundary Conditions

Let the vortex-core radius at x=0 be r=1, and let the radius of the farfield boundary be r=R. The inflow properties used here to model the vortex at x=0 have been used by several investigators.[7,8,11] They are:

$$\begin{aligned} u(r) &= 0 \\ v(r) &= Vr(2-r^2) \qquad 0 \le r \le 1 \\ v(r) &= V/r \qquad 1 \le r \le R \\ w(r) &= 1 \end{aligned} \tag{9}$$

where V, the swirl parameter, is the circumferential velocity at the edge of vortex core. V measures the strength of the incoming vortex. Like Re, it is a free parameter of the problem.

Along the vortex axis, r=0, the boundary conditions are

$$\begin{aligned} u(x) &= 0 \\ v(x) &= 0 \\ w_r(x) &= 0 \end{aligned} \tag{10}$$

In the farfield, r=R, the boundary conditions are

$$\begin{aligned} w_r - u_x &= 0 \\ v(x) &= V/R \\ w(x) &= 1. \end{aligned} \tag{11}$$

At the outflow boundary, x=L, the boundary conditions are

$$\begin{aligned} u_x(r) &= 0 \\ v_x(r) &= 0 \\ u_r(r) + w_x(r) + \frac{u(r)}{r} &= 0 \end{aligned} \tag{12}$$

The pressure level of the flowfield is specified by fixing the pressure in one cell.

Solution Procedure

The discretized governing equations and the boundary conditions represents a system of the form

$$J\Delta\phi = -R \tag{13}$$

where J is the Jacobian matrix, $\Delta\phi$ is the correction vector and R is the residual vector. Equation (13) is solved by performing an LU decomposition of the Jacobian matrix, Gaussian elimination and Newton iteration. Since J is a function of the solution, LU decomposition of the Jacobian matrix is performed at every iteration.

For the case of Re = 100 the initial flowfield was set equal to the inflow conditions. For Reynolds numbers higher than 100 the converged solution for the previous lower Reynolds number was used as the initial condition.

For a mesh with Imax points in the x-direction and Jmax points in the r-direction, the Jacobian matrix has a bandwidth approximately equal to 8 Jmax. The storage requirement is approximately equal to $32\,\text{Jmax}^2\,\text{Imax}$. Here Jmax is smaller than Imax. For a mesh with Imax = 401 and Jmax = 33, a single matrix inversion requires approximately 47 seconds on the NAS Cray-2 computer. Typically, about 5 to 8 inversions are needed to account for the nonlinearity and achieve machine accuracy. A typical convergence history is shown in figure 2. The asymptotic convergence rate is quadratic. Note that, because the continuity equation is linear, its residual is zero after the first inversion. This does not imply a good solution after one step, but a balancing of errors for Δu, Δv and Δw such as to satisfy the equation.

Three Dimensional Problem

In the second part of the study, the first attempt is made to solve the three-dimensional problem. With the computer resources currently available, it is not possible to solve directly the whole set of coupled equations for the full three-dimensional space. Hence the dependent variables are expanded in the azimuthal direction using Fourier transforms, namely:

$$\phi = \begin{bmatrix} u \\ v \\ w \\ p \end{bmatrix} = \phi_0 + \sum_{m=1}^{N} \bar{\phi}_m \cos(m\theta) + \sum_{m=1}^{N} \tilde{\phi}_m \sin(m\theta) \tag{14}$$

where

$$\begin{aligned} \phi_0 &= \phi_0(r,x) \\ \bar{\phi}_m &= \bar{\phi}_m(r,x) \\ \tilde{\phi}_m &= \tilde{\phi}_m(r,x) \end{aligned} \tag{15}$$

Retaining only the first two Fourier components and neglecting higher order terms, yields 12 equations in 12 unknowns. Dropping the subscript for convenience, these equations are

$$u_r + w_x + \frac{u}{r} = 0 \tag{16}$$

$$\bar{u}_r + \bar{w}_x + \frac{\bar{u}+\tilde{v}}{r} = 0 \tag{17}$$

$$\tilde{u}_r + \tilde{w}_x + \frac{\tilde{u}-\bar{v}}{r} = 0 \tag{18}$$

$$\mathbf{q}.\nabla u + p_r - \frac{v^2}{r} = \frac{1}{Re}\left[\nabla^2 u - \frac{u}{r^2}\right] \tag{19}$$

$$\mathbf{q}.\nabla\bar{u} + \bar{\mathbf{q}}.\nabla u + \bar{p}_r + \frac{v(\tilde{u}-2\bar{v})}{r} = \frac{1}{Re}\left[\nabla^2\bar{u} - \frac{2(\bar{u}+\tilde{v})}{r^2}\right] \tag{20}$$

$$\mathbf{q}.\nabla\tilde{u} + \tilde{\mathbf{q}}.\nabla u + \tilde{p}_r - \frac{v(\bar{u}+2\tilde{v})}{r} = \frac{1}{Re}\left[\nabla^2\tilde{u} - \frac{2(\tilde{u}-\bar{v})}{r^2}\right] \tag{21}$$

$$\mathbf{q}.\nabla v + \frac{uv}{r} = \frac{1}{Re}\left[\nabla^2 v - \frac{v}{r^2}\right] \tag{22}$$

$$\mathbf{q}.\nabla\bar{v} + \bar{\mathbf{q}}.\nabla v + \frac{\tilde{p}}{r} + \frac{v(\bar{u}+\tilde{v})}{r} + \frac{u\bar{v}}{r} = \frac{1}{Re}\left[\nabla^2\bar{v} + \frac{2(\tilde{u}-\bar{v})}{r^2}\right] \tag{23}$$

$$\mathbf{q}.\nabla\tilde{v} + \tilde{\mathbf{q}}.\nabla v - \frac{\bar{p}}{r} + \frac{v(\tilde{u}-\bar{v})}{r} + \frac{u\tilde{v}}{r} = \frac{1}{Re}\left[\nabla^2\tilde{v} - \frac{2(\bar{u}+\tilde{v})}{r^2}\right] \tag{24}$$

$$\mathbf{q}.\nabla w + p_x = \frac{1}{Re}\left[\nabla^2 w\right] \tag{25}$$

$$\mathbf{q}.\nabla\bar{w} + \bar{\mathbf{q}}.\nabla w + \bar{p}_x + \frac{v\tilde{w}}{r} = \frac{1}{Re}\left[\nabla^2\bar{w} - \frac{\bar{w}}{r^2}\right] \tag{26}$$

$$\mathbf{q}.\nabla\tilde{w} + \tilde{\mathbf{q}}.\nabla w + \tilde{p}_x - \frac{v\bar{w}}{r} = \frac{1}{Re}\left[\nabla^2\tilde{w} - \frac{\tilde{w}}{r^2}\right] \tag{27}$$

where

$$\begin{bmatrix} \mathbf{q} \\ \bar{\mathbf{q}} \\ \tilde{\mathbf{q}} \end{bmatrix} = \begin{bmatrix} u \\ \bar{u} \\ \tilde{u} \end{bmatrix}\hat{r} + \begin{bmatrix} w \\ \bar{w} \\ \tilde{w} \end{bmatrix}\hat{x} \tag{28}$$

$$\nabla = \frac{\partial}{\partial r}\hat{r} + \frac{\partial}{\partial x}\hat{x} \tag{29}$$

$$\nabla^2 = \frac{\partial^2}{\partial r^2} + \frac{1}{r}\frac{\partial}{\partial r} + \frac{\partial^2}{\partial x^2} \tag{30}$$

Equations (16), (19), (22) and (25) represent the axisymmetric model. Equations (17), (18), (20), (21), (23), (24), (26) and (27) give the contribution of the first Fourier mode. The first mode represents the most significant three-dimensional effect, particularly, it will show how stable the axisymmetric solutions are to three-dimensional perturbations.

Boundary Conditions

The boundary conditions are similar to the ones used in the axisymmetric case except at the axis. Along the axis , r=0, the boundary conditions are

$$\begin{aligned} \bar{u}+\tilde{v} &= 0 \\ \tilde{u}-\bar{v} &= 0 \\ \bar{u}_r+\tilde{v}_r &= 0 \\ \tilde{u}_r-\bar{v}_r &= 0 \\ \bar{w} &= 0 \\ \tilde{w} &= 0 \end{aligned} \qquad (31)$$

Solution Procedure

These equations are solved in the following manner. Starting with the symmetric solution ϕ_0, and slightly perturbed inflow conditions, the eight equations representing the first Fourier mode are solved simultaneously by direct inversion for $\bar{\phi}_1$ and $\tilde{\phi}_1$. Since these equations are linear, only one inversion is necessary to obtain a solution.

However, since there are eight coupled equations the bandwidth of the matrix is approximately equal to 16 Jmax and the storage requirement is approximately equal to $128\,\text{Jmax}^2\,\text{Imax}$. For a mesh with Imax=241 and Jmax=33, a single matrix inversion takes about 213 seconds on the NAS Cray-2 computer.

Results

Axisymmetric Case

Several accuracy checks were performed to determine the appropriate requirements for mesh resolution and boundary location. To obtain a mesh-independent solution, it was found that the mesh spacing Δx and Δr should be less than or equal to 1/16. A mesh spacing of 1/16 in the x and r directions was used in this study. Location of the farfield at R=2 was found to be sufficient to minimize the influence of the farfield boundary. It was found that the location of the outflow boundary is directly related to the Reynolds number since as the Reynolds number increases, more and more structure develops downstream along the axial direction. Surprisingly, the upstream flow structure freezes as the Reynolds number increases. For all the cases that are considered here, the outflow was located at L=25. With the outflow at this location, good quantitative representation of the solution is obtained for all the Reynolds numbers considered here (Re=100 to Re=1500). For low Reynolds numbers, it is possible to obtain accurate solutions with a domain of shorter length.

Figure 3 shows the streamline patterns for Reynolds numbers, Re, ranging from 100 to 1500 and swirl parameter, V of 0.9 and 1.0. As the Reynolds number is increased, more and more breakdown structures develop. Multiple breakdowns have been observed experimentally by Harvey[5]. The flow structure is also very sensitive to small variations of the swirl parameter. For V=0.9, as the Reynolds number is increased, more and more recirculating zones appear along the axis. For V=1.0 the first bubble lifts off the axis at about Re=500, forming a toroidal recirculating zone. As the Reynolds number is increased further, the second bubble elongates and necks in the middle. At about Re=600, the second bubble breaks into two, forming a third recirculating zone.

Figure 4 shows the vorticity contours for the flowfields shown in Figure 3. One interesting feature of the vorticity field is that as the Reynolds number is increased, the vorticity intensifies at the spot where breakdown is to occur, thus signalling the appearance of a bubble. For example, in figure 4 we can see the appearance of a second region of high vorticity at Re=200. As the Reynolds number is increased, the concentration of vorticity in this region also increases and eventually a second breakdown occurs at Re=400 (Figure 3).

Figures 5 and 6 show the map of the axial velocity, w, along the axis for V=0.9 and V=1.0 respectively on a Reynolds-number, axial-location plane. The hatched areas show the regions of negative w. It is clear that near the inflow, the flow asymptotes to a flow field invariant with Reynolds number. In figure 6, where V=1.0, it can be seen that the first bubble lifts off the axis around Re=500. The second bubble breaks up into two around Re=600 and it lifts off the axis around Re=850.

All these results agree qualitatively with the results from the streamfunction - vorticity formulation presented in reference 10. Since there are differences in the boundary conditions in the two approaches, quantitative comparison is difficult.

Three Dimensional Case

In this section a few representative results are presented illustrating the sensitivity of the axisymmetric solutions to three dimensional perturbations. Starting with the steady-state solution of the axisymmetric problem, the equations for the first Fourier component are solved with a perturbed (non-axisymmetric) boundary condition. In all the cases that are discussed here, the perturbation at the boundary is introduced through a harmonic variation in the w velocity component with a maximum amplitude of 0.1%. The calculations are done on a domain shorter than the one used in the previous section. This was necessary because of the large memory and intense computing requirements of the three dimensional problem. However, the lengths of the domains selected for the cases presented were all sufficiently large to obtain accurate solutions at the Reynolds number indicated.

The magnitude of the total velocity is,

$$q = \sqrt{u^2+v^2+w^2} \qquad (32)$$

where u,v and w are given by equation 8 for m=1. The magnitude of the axisymmetric component of the velocity is,

$$q_0 = \sqrt{u_0^2+v_0^2+w_0^2} \qquad (33)$$

We define a perturbation velocity $\bar{q}$ by,

$$\bar{q} = q-q_0 \qquad (34)$$

Contours of the magnitude of total velocity q and perturbation velocity $\bar{q}$ are plotted on r–θ planes at selected axial locations. At these locations, the r–θ planes cut through the recirculating zones. These locations are marked on figure 3. Figure 7a shows the contours of q on the r–θ plane at an axial location x=2.5 (plane AA in figure 3) for Re=200 and V=0.9. A small deviation from the axisymmetric solution can be noticed. (Compare outer contour with outer circular boundary indicated by dash line.) Figure 7b shows the contours of $\bar{q}$ at the same location. The maximum magnitude of $\bar{q}$ is about an order-of-magnitude less than the magnitude of the axisymmetric component. In figures 8a and 8b, the contours of q and $\bar{q}$, respectively, are shown for the case Re=500 and V=0.9 at an axial location of x=2.0 (plane BB in figure 3). The features shown here are very similar to those shown in figure 7. In figures 9a and 9b, we show again the contours of q and $\bar{q}$ for the same case, but at an axial location x=6.5 (plane CC in figure 3). A large deviation from the axisymmetric solution can be observed in figure 9. The magnitude of the perturbation velocity in figure 9b is of the same order as the magnitude of the axisymmetric component. It appears that small perturbations remain small at low Reynolds numbers. However the perturbations can become significant as the Reynolds number is increased. In order to validate these solutions, the contributions due to higher Fourier modes need to be investigated. Inclusion of higher modes into the present algorithm leads to a formidably large and expensive problem to solve. Currently, we are looking again at iterative techniques to solve the full three dimensional problem.

Concluding Remarks

Numerical solution of the steady Navier-Stokes equations were obtained for the vortex breakdown phenomenon for Reynolds number ranging from 100 to 1500 and swirl velocity parameter, V, of 0.9 and 1.0. The solutions were very sensitive to changes in V. It was found that near the inflow the solutions become independent of Reynolds number and that downstream more and more structure appears as the Reynolds number is increased. Vorticity contours signaled the occurrence of a breakdown. All these solutions agreed , qualitatively, with the ones obtained using a streamfunction - vorticity formulation.

The first Fourier component indicates a relatively small effect on the axisymmetric solution, due to three dimensional perturbation, at low Reynolds numbers. It indicates a significant effect at higher Reynolds numbers. Higher Fourier modes have to be evaluated to understand the three-dimensional problem.

References

1. D.H. Peckham and S. A. Atkinson, "Preliminary Results of Low Speed Wind Tunnel Tests on a Gothic Wing of Aspect Ratio 1.0, " Aeronautical Research Council, CP508, 1957.

2. M.G. Hall, "Vortex Breakdown," Annual Review of Fluid Mechanics, Vol. 4, 1972, pp. 195-218.

3. S. Leibovich, "The Structure of Vortex Breakdown," Annual Review of Fluid Mechanics, Vol. 10, 1978, pp. 221-246

4. S. Leibovich, "Vortex Stability and Breakdown: Survey and Extension," AIAA Journal, Vol. 22, No. 9, 1984, pp. 1192-1206.

5. J.K. Harvey, "Some Observations of the Vortex Breakdown Phenomenon," Journal of Fluid Mechanics, Vol. 14, 1962, pp. 585-592.

6. T.B. Benjamin, "Theory of the Vortex Breakdown Phenomenon", Journal of Fluid Mechanics, Vol. 14, 1962, pp. 593-629.

7. W.J. Grabowski and S.A. Berger, "Solution of the Navier-Stokes Equations for Vortex Breakdown," Journal of Fluid Mechanics, Vol. 75, Part 3, 1976, pp. 525-544.

8 M. Hafez, G. Kuruvila, and M.D. Salas, "Numerical Study of Vortex Breakdown," Applied Numerical Mathematics, Vol. 2, 1986, pp. 291-302.

9. M. Hafez, J. Ahmad, G. Kuruvila, and M.D. Salas, "Vortex Breakdown Simulation" AIAA Paper No. 87-1343, AIAA 19th Fluid Dynamics, Plasma Dynamics, and Lasers Conference, June 8-10, 1987, Honolulu, Hawaii

10. M.D. Salas, and G. Kuruvila, "Vortex Breakdown Simulation: A Circumspect Study of the Steady Laminar Axisymmetric Model," The Symposium on Physical Aspects of Numerical Gas Dynamics, August 12-13, 1987, Farmingdale, New York.

11. P.S. Beran, "Numerical Simulation of Trailing Vortex Bursting", AIAA Paper No. 87-1313, AIAA 19th Fluid Dynamics, Plasma Dynamics, and Lasers Conference, June 8-10, 1987, Honolulu, Hawaii

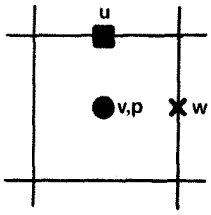

Figure 1. Mesh.

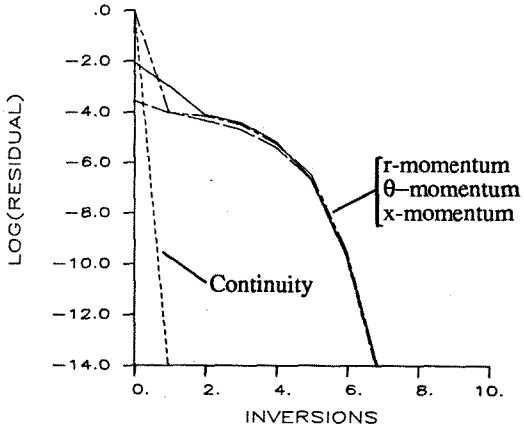

Figure 2. Convergence History.

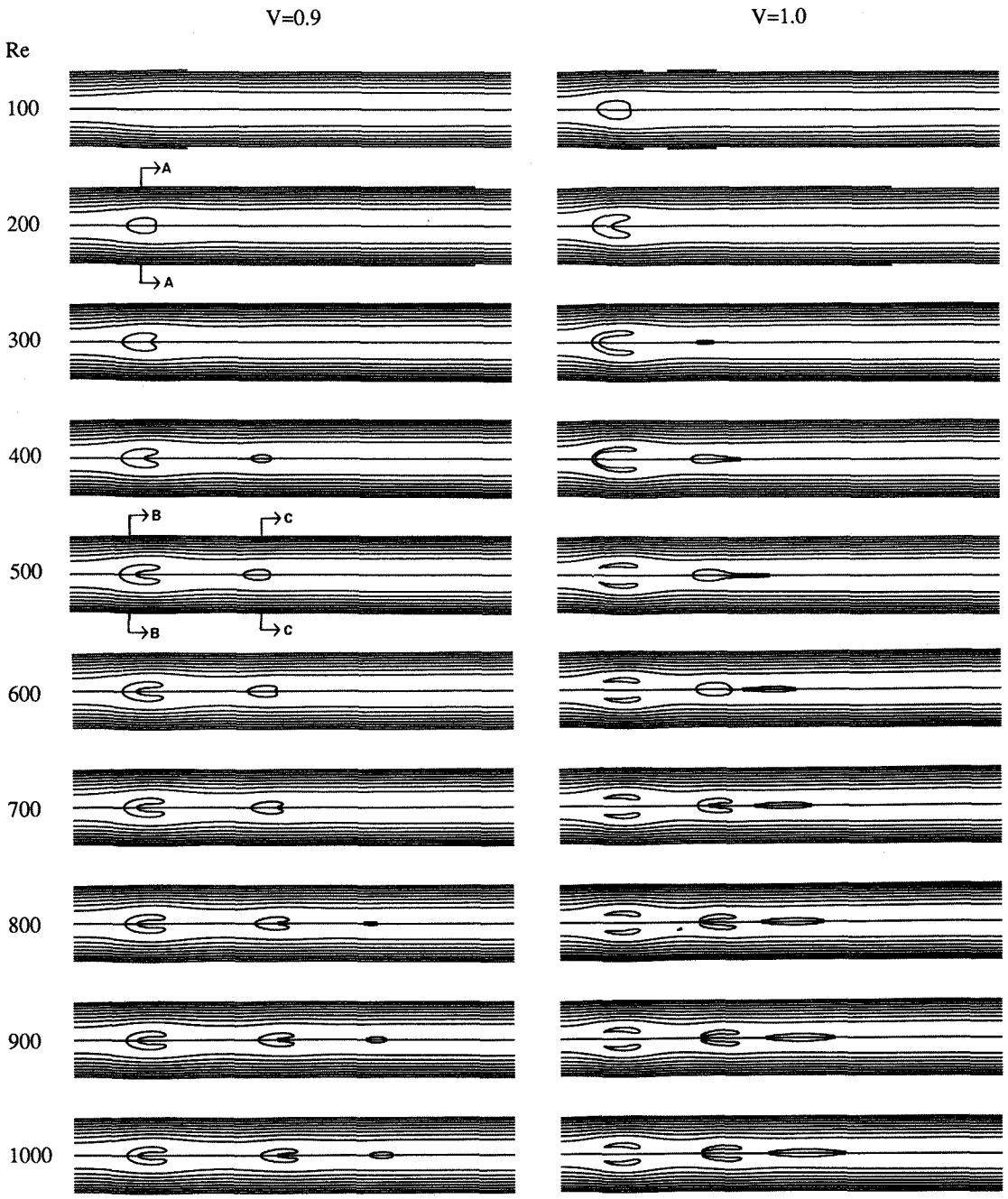

Figure 3. Computed Streamline Patterns. L=25, (plotted up to x=15) and R=2.

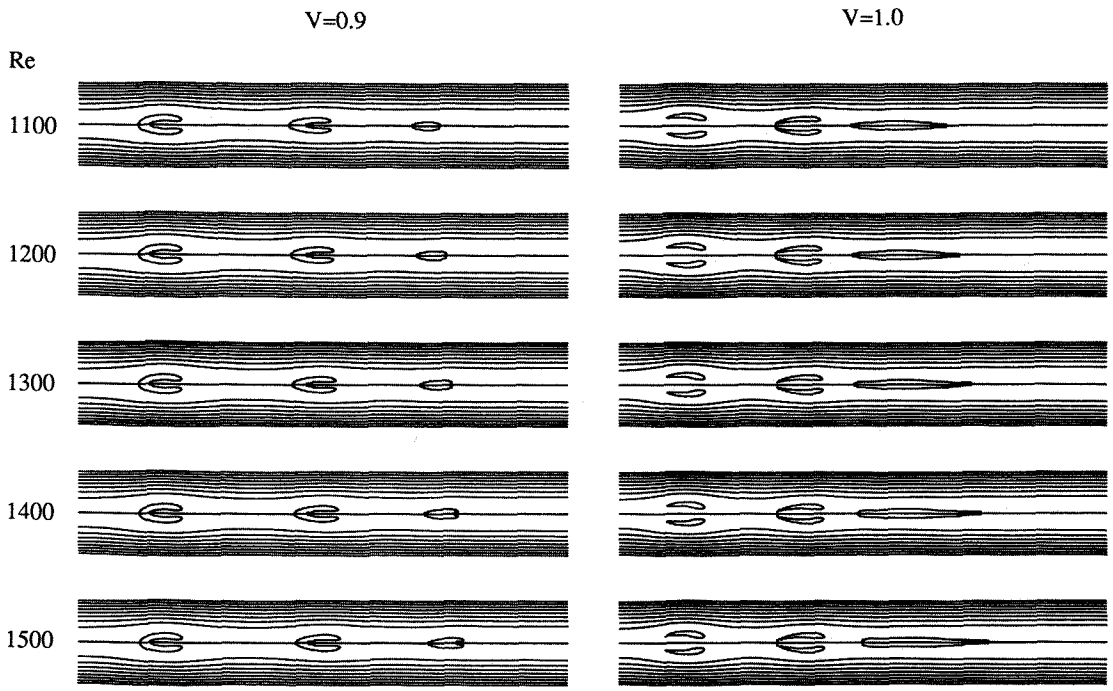

Figure 3. Concluded

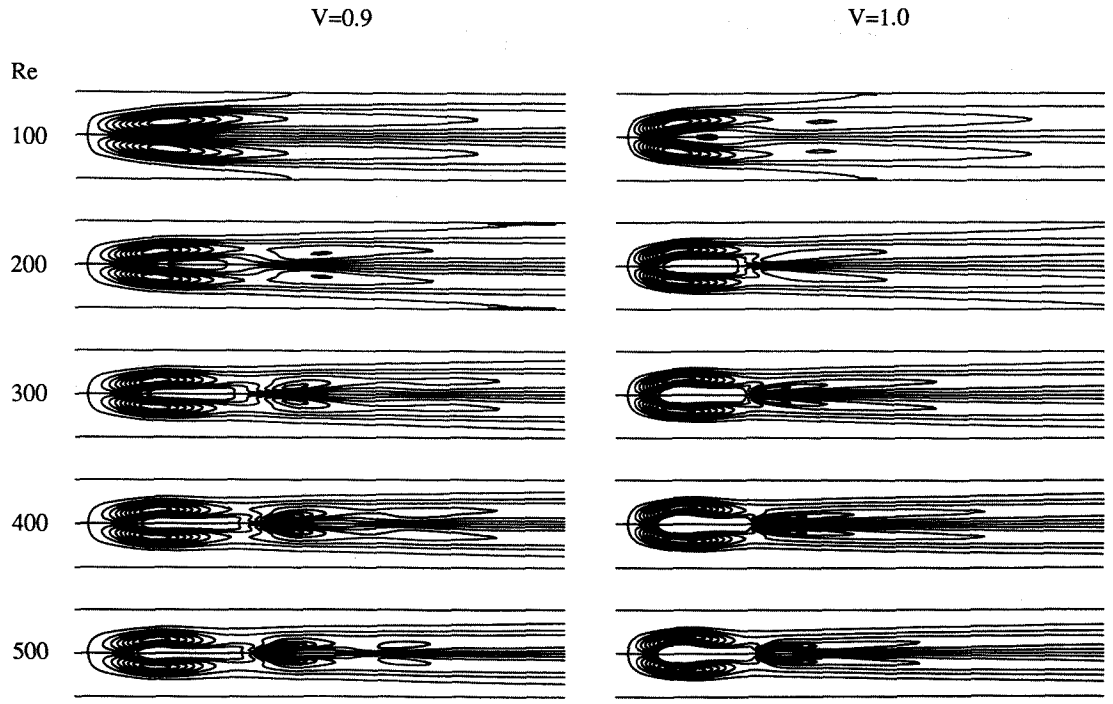

Figure 4. Computed Vorticity Patterns. L=25, (plotted up to x=15) and R=2.

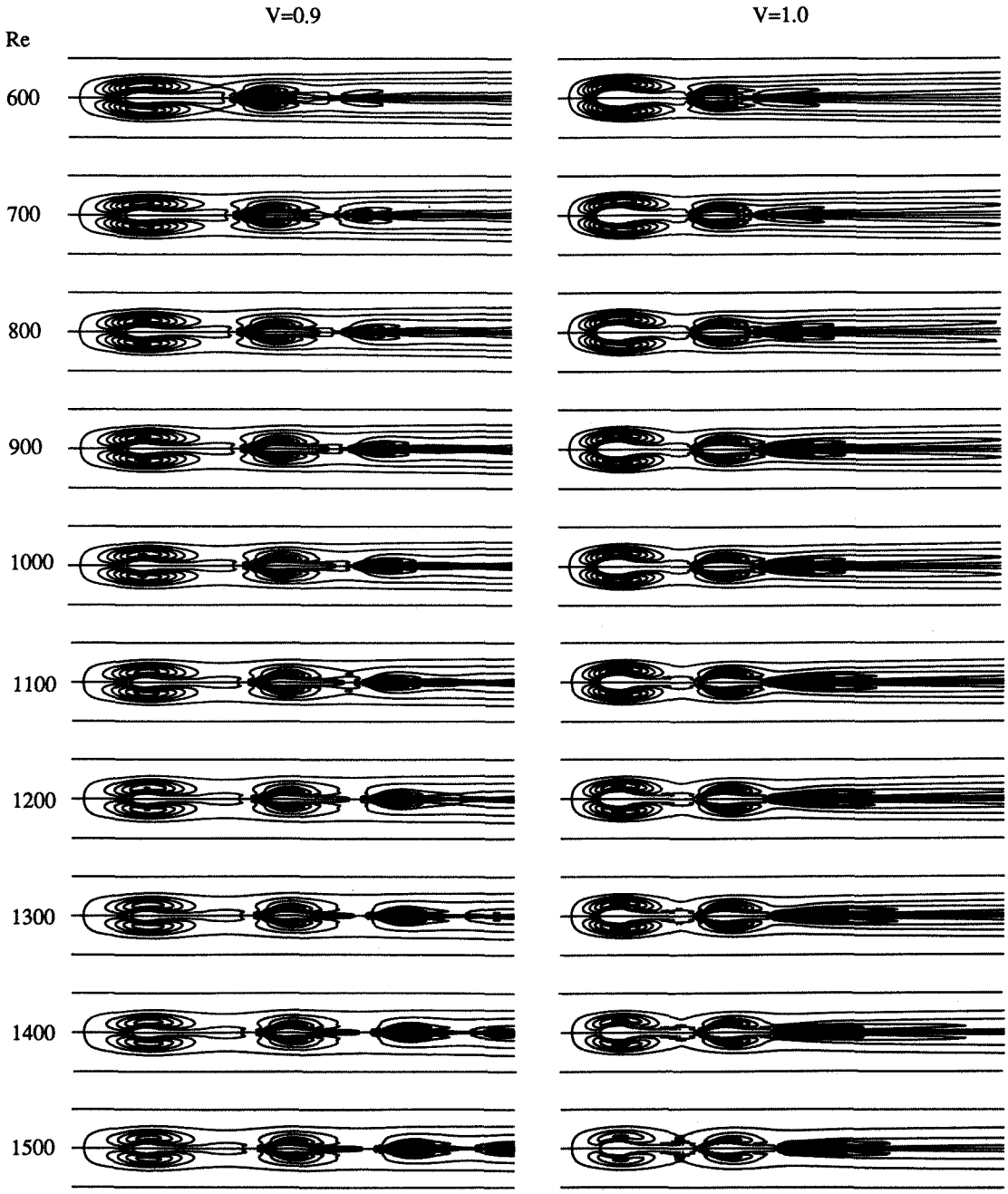

Figure 4. Concluded

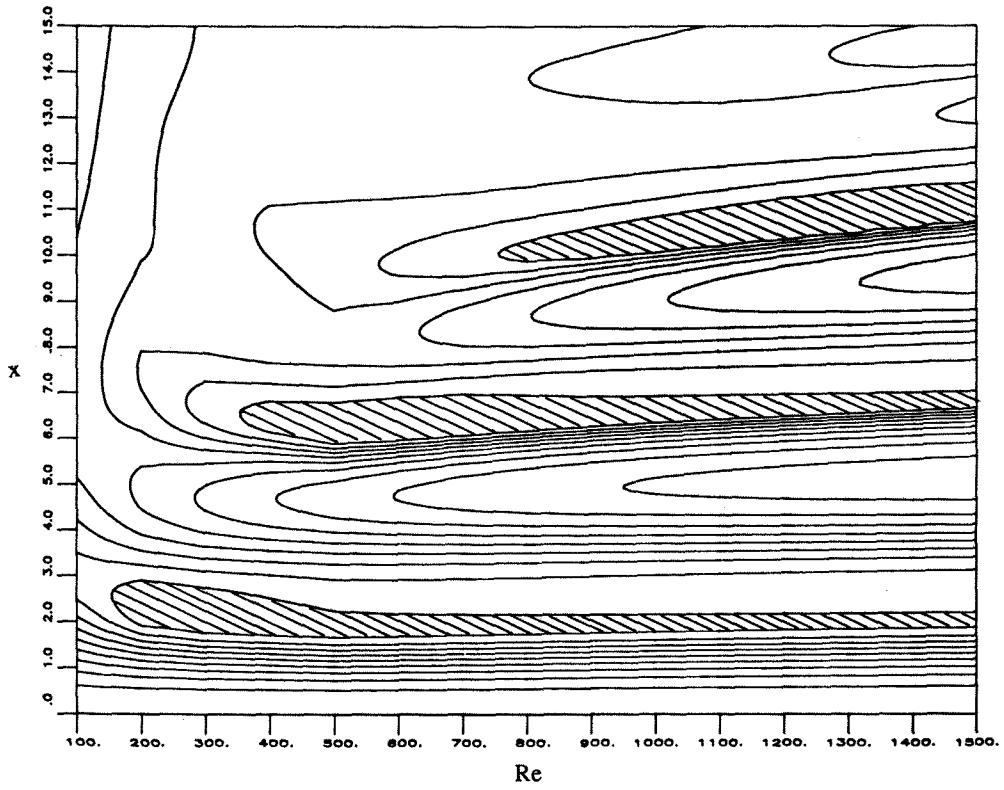

Figure 5. Map of Axial Velocity along the axis for V = 0.9

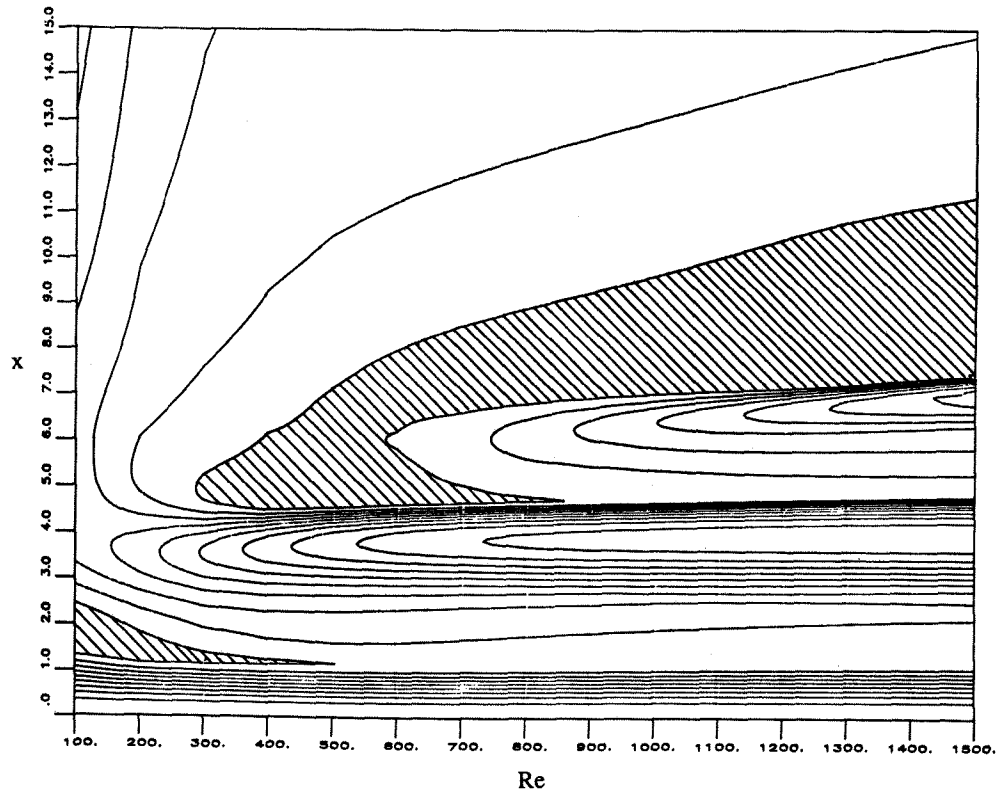

Figure 6. Map of Axial Velocity along the axis for V = 1.0

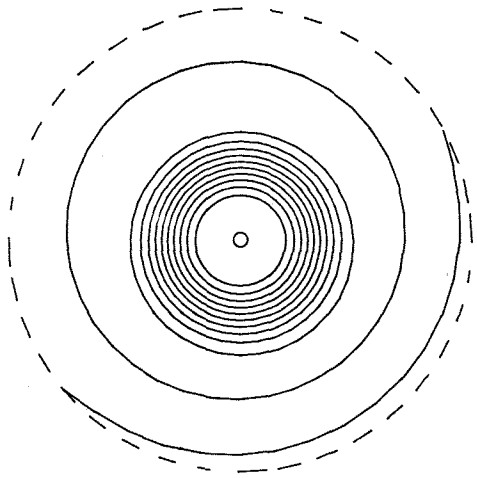

Figure 7a. Contours of q for Re=200 and V=0.9 at x=2.5.

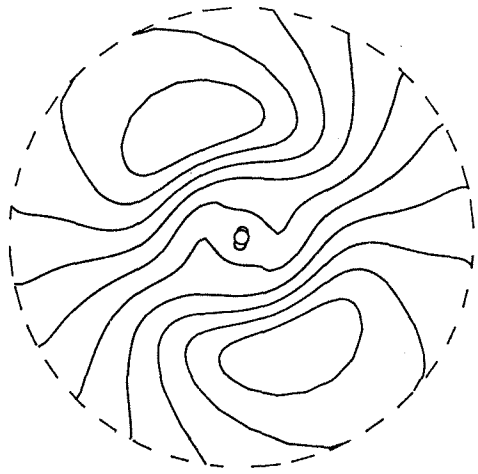

Figure 7b. Contours of $\overline{q}$ for Re=200 and V=0.9 at x=2.5.

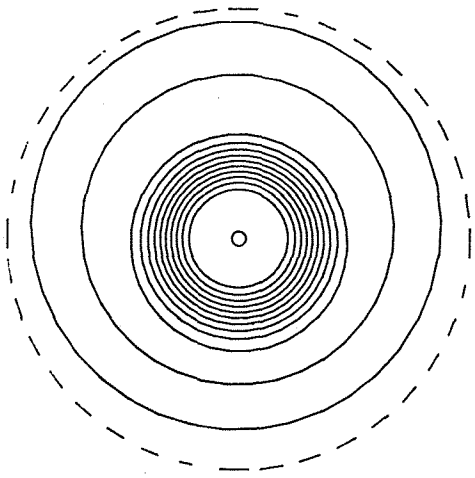

Figure 8a. Contours of q for Re=500 and V=0.9 at x=2.0.

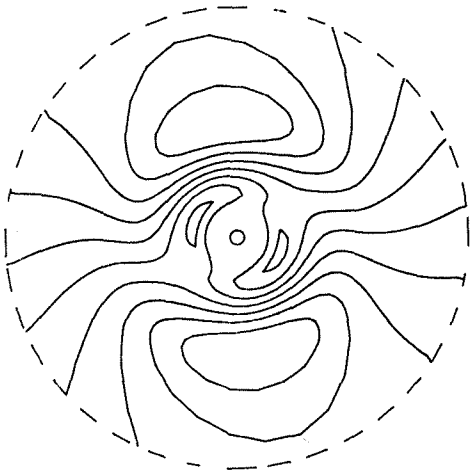

Figure 8b. Contours of $\overline{q}$ for Re=500 and V=0.9 at x=2.0.

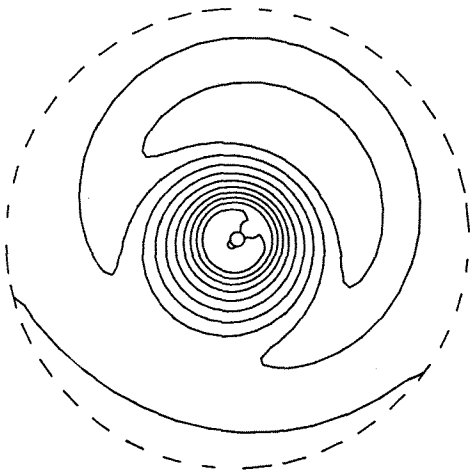

Figure 9a. Contours of q for Re=500 and V=0.9 at x=6.5.

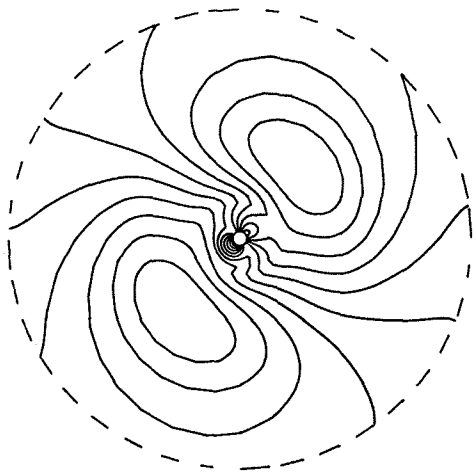

Figure 9b. Contours of $\overline{q}$ for Re=500 and V=0.9 at x=6.5.